Journal Name

Dynamic Article Links ►

Cite this: DOI: 10.1039/c0xx00000x

www.rsc.org/xxxxxx

ARTICLE TYPE

Systematic Modulation and Enhancement of CO_2:N_2 Selectivity and Water Stability in an Isoreticular Series of Bio-MOF-11 Analogues

Tao Li,[a] De-Li Chen,[b] Jeanne E. Sullivan,[a] Mark T. Kozlowski,[a] J. Karl Johnson,[bc] and Nathaniel L. Rosi*[a]

Received (in XXX, XXX) Xth XXXXXXXXX 20XX, Accepted Xth XXXXXXXXX 20XX
DOI: 10.1039/b000000x

An isoreticular series of cobalt-adeninate bio-MOFs (**bio-MOFs 11-14**) is reported. The pores of **bio-MOFs 11-14** are decorated with acetate, propionate, butyrate, and valerate, respectively. The nitrogen (N_2) and carbon dioxide (CO_2) adsorption properties of these materials are studied and compared. The isosteric heats of adsorption for CO_2 are calculated, and the CO_2:N_2 selectivities for each material are determined. As the lengths of the aliphatic chains decorating the pores in **bio-MOFs 11-14** increase, the BET surface areas decrease from 1148 m^2/g to 17 m^2/g while the CO_2:N_2 selectivities predicted from ideal adsorbed solution theory at 1 bar and 273 K for a 10:90 CO_2:N_2 mixture range from 73:1 for **bio-MOF-11** to 123:1 for **bio-MOF-12** and finally to 107:1 for **bio-MOF-13**. At 298 K, the selectivities are 43:1 for **bio-MOF-11**, 52:1 for **bio-MOF-12**, and 40:1 for **bio-MOF-13**. Additionally, it is shown that **bio-MOF-14** exhibits a unique molecular sieving property that allows it to adsorb CO_2 but not N_2 at 273 and 298 K. Finally, the water stability of **bio-MOFs 11-14** increases with increasing aliphatic chain length. **Bio-MOF-14** exhibits no loss of crystallinity or porosity after soaking in water for one month.

INTRODUCTION

CO_2 capture from flue gas of coal-fired power plants is recognized as an important clean energy goal, and the development of new adsorbent materials for selective CO_2 capture is central to this pursuit.[1, 2] Metal-organic frameworks (MOFs) are being intensively studied as CO_2 adsorbents because of their tailorable structures and chemical functionality and their physisorptive property, an aspect that is expected to decrease adsorbent regeneration energy and therefore net energy costs.[3, 4]

To first be considered for CO_2-capture applications, a MOF adsorbent must meet several important criteria: i) it should have a high capacity for CO_2 at flue gas temperatures; ii) it should selectively adsorb CO_2 over N_2; and iii) its structure should be able to withstand the moisture present in flue gas. Numerous MOFs meet at least one of these criteria, yet few meet all of these criteria.[5-24]

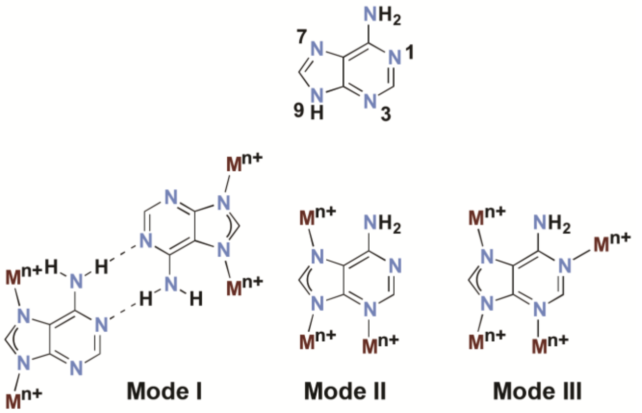

Figure 1. Coordination modes of adenine.

We have introduced and developed a strategy for preparing CO_2-phillic MOFs that utilizes the nucleobase adenine as a linker molecule. Adenine is an ideal linker because it has multiple Lewis-basic sites that can interact with CO_2. In principle, by controlling the adenine coordination mode, one should be able to control the number of Lewis-basic sites exposed to the pore space within the MOF. In our work[10, 25-29], we identified three principle coordination modes (Figure 1) for deprotonated adenine (adeninate) within finite and infinite periodic coordination assemblies. Mode I, observed in 0-D macrocyclic structures[26], and Mode III, observed in **bio-MOF-1**[27-29] and **bio-MOF-100**[25], have only one free Lewis-basic site (N3 and the amino group, respectively) , while Mode II, observed in **bio-MOF-11**[10], has two free Lewis-basic sites (N1, and the amino group). Of these reported materials, **bio-MOF-11**, as expected, had the highest capacity for CO_2 and a high selectivity for CO_2 over N_2. In fact, compared to other reported MOFs, **bio-MOF-11** remains one of the best adsorbents for CO_2 in terms of capacity and selectivity.[3] However, despite its favorable CO_2 capacity and selectivity, it degrades rapidly in water and therefore would not withstand the moisture present in flue gas (5~7 % water[3]). In this report, we present a strategy for tuning the CO_2 adsorption properties and the water stability of a series of new isostructural **bio-MOF-11** analogues, hereafter named **bio-MOF-12**, **13**, and **14**. We modulate the porosity and hydrophobicity within this series by decorating the pores with different aliphatic monocarboxylates. Importantly, we demonstrate that one member of this series, **bio-MOF-14**, is highly stable in water and exhibits exceptional selectivity for CO_2 over N_2, due to a molecular sieving effect.

EXPERIMENTAL SECTION

Reagents and General Methods.

N,N'-dimethylformamide (DMF) was dried over 3 Å molecular sieves for 1 day prior to use. Other chemicals were obtained via commercial sources and used directly without further purification. Nanopure water (18.2 MΩ) was obtained using a Barnstead DiamondTM System.

Elemental microanalyses (EA) were performed by the University of Illinois, Department of Chemistry Microanalytical Laboratory using a Perkin-Elmer 240 Elemental Analyzer and an Exeter Analytical CE440.

Thermogravimetric analysis (TGA) was conducted on a TGA Q500 thermal analysis system. Prior to analysis, samples were dried under argon flow (UHP) until the powder could move around freely. Approximately 5 mg of sample was loaded into a platinum pan and heated under a constant N_2 (UHP) flow from room temperature to 600 °C at a rate of 5 °C/min. Data were analyzed using the TA Universal Analysis software package.

Powder X-ray diffraction (PXRD) patterns were collected using a Bruker AXS D8 Discover powder diffractometer equipped with a Cu Kα X-ray source at 40 kV, 40 mA. Scan speed and step size were set at 0.2 sec/step and 0.02 °/step respectively. Generally, MOF samples were spread evenly on a glass slide and data were collected from $4° < 2\theta < 45°$. Simulated powder patterns from single-crystal X-ray diffraction data were generated using Mercury 3.0 software.

Scanning Electron Microscopy (SEM) images were taken using a Philips XL-30 field emission scanning electron microscope under BSE mode.

Preparation of Cobalt Salts.

Cobalt carbonate powder (1.19 g, 10 mmol) was suspended in nanopure water (50 ml). An aliphatic acid (~12 mmol, 1.2 equivalents) was added slowly to the suspension. Heat and stirring were required to fully dissolve the cobalt carbonate solid. Once the cobalt carbonate solid was dissolved, the reaction flask was heated in an oven (100 °C overnight) to remove water, yielding a purple solid. Yield: Co propionate, 1.93 g (94 %); products contained some water and CoO, as determined by EA. Anal. Calcd. for $Co(C_2H_5CO_2)_2$ (with 0.11 CoO and 0.33 H_2O impurity): C, 32.85; H, 4.90; N, 0.00. Found: C, 32.74; H, 4.74; N, 0.095; Co butyrate, 2.14 g (92 %). Anal. Calcd. for $Co(C_3H_7CO_2)_2$ (with 0.33 CoO and 0.53 H_2O impurity): C, 35.89; H, 5.67; N, 0.00. Found: C, 35.86; H, 5.615; N, 0.1; Co valerate, 2.22 g (85 %). Anal. Calcd. for $Co(C_4H_9CO_2)_2$ (with 0.05 CoO and 0.53 H_2O impurity): C, 43.74; H, 6.99; N, 0.00. Found: C, 43.64; H, 6.83; N, 0.12.

Synthesis of Bio-MOF-11.

Stock solutions of cobalt acetate (0.05 M) and adenine (0.05 M) in pre-dried DMF were prepared. To a Schlenk tube (40 mL) were added cobalt acetate solution (9.0 mL; 0.45 mmol), adenine solution (27.0 mL; 1.35 mmol), and nanopure water (120 µL). After the solution was frozen in liquid nitrogen and evacuated to 200 mTorr, it was heated in a 130 °C oven (24 h). Black, octahedral crystals were collected, washed (dry DMF, 3X), and dried under argon flow. Yield: 102 mg, 90 % (based on cobalt acetate salt). Anal. Calcd. for $Co_2(ad)_2(CH_3CO_2)_2 \bullet 2.25$ DMF, 0.6 H_2O (ad = adeninate): C, 36.68; H, 4.59; N, 25.25. Found: C, 36.70; H, 4.06; N, 25.205.

Synthesis of Bio-MOF-12.

Stock solutions of cobalt propionate (0.05 M) and adenine (0.05 M) in pre-dried DMF were prepared. To a Schlenk tube (40 mL) were added cobalt propionate solution (9.0 mL; 0.45 mmol), adenine solution (27.0 mL; 1.35 mmol), and nanopure water (120 µL). After the solution was frozen in liquid nitrogen and evacuated to 200 mTorr, it was heated in a 130 °C oven (24 h). Black, octahedral crystals were collected, washed (dry DMF, 3X), and dried under argon flow. Yield: 94 mg, 78 % (based on Co propionate). Anal. Calcd. for $Co_2(ad)_2(C_2H_5CO_2)_2 \bullet 2.25$ DMF, 0.3 H_2O: C, 38.92; H, 4.93; N, 24.44. Found: C, 38.99; H, 4.59; N, 24.36.

Synthesis of Bio-MOF-13.

Stock solutions of cobalt butyrate (0.05 M) and adenine (0.05 M) in pre-dried DMF were prepared. To a Schlenk tube (40 mL) were added cobalt valerate solution (9.0 mL; 0.45 mmol), adenine solution (27.0 mL; 1.35 mmol), and nanopure water (120 µL). After the solution was frozen in liquid nitrogen and evacuated to 200 mTorr, it was heated in a 130 °C oven (24 h). Black, octahedral crystals were collected, washed (dry DMF, 3X), and dried under argon flow. Yield: 90 mg, 71 % (based on Co butyrate). Anal. Calcd for $Co_2(ad)_2(C_3H_7CO_2)_2 \bullet 1.1$ DMF, 0.6 H_2O: C, 39.27; H, 4.78; N, 23.86. Found: C, 39.36; H, 4.185; N, 23.74.

Synthesis of Bio-MOF-14.

Stock solutions of cobalt valerate (0.05 M) and adenine (0.05 M) in pre-dried DMF were prepared. To a Schlenk tube (40 mL) were added cobalt valerate solution (9.0 mL; 0.45 mmol), adenine solution (27.0 mL; 1.35 mmol), and nanopure water (120 µL). After the solution was frozen in liquid nitrogen and evacuated to 200 mTorr, it was heated in a 130 °C oven (24 h). Black, octahedral crystals were collected, washed (dry DMF, 3X), and dried under argon flow. Yield: 85 mg, 64 % (based on Co valerate). Anal. Calcd for $Co_2(ad)_2(C_4H_9CO_2)_2 \bullet 0.6$ DMF, 0.6 H_2O: C, 40.72; H, 4.92; N, 23.09. Found: C, 40.8; H, 4.63; N, 22.93.

Gas Adsorption Measurements and Isosteric Heats of Adsorption.

Gas adsorption isotherms were collected using a Quantachrome Autosorb-1 instrument. As synthesized crystals were thoroughly washed with anhydrous dichloromethane and dried under argon flow. Approximately 60 mg of each sample was added into a pre-weighed sample analysis tube. The samples were degassed at 100 °C under vacuum for 24-48 hours until the pressure change rate was no more than 3.5 mTorr/min. A liquid N_2 bath was used for the N_2 adsorption experiments at 77 K. A water/ethylene glycol bath was used for isotherms collected at

273 K, 298 K, 303 K, 308 K, and 313 K. BET surface areas were calculated using N_2 isotherms at 77 K. UHP grade N_2 and CO_2 gas adsorbates (99.999 %) were used in this study.

CO_2 adsorption isotherms of **bio-MOF-11** to **14** at different temperatures (273 K, 298 K, 303 K, 308 K and 313 K) were fit to the dual site Langmuir model.[30] The isosteric heat of adsorption values were calculated using the Clausius-Clapeyron equation. Details are included in the Supporting Information.

Water Stability Experiments.

Approximately 100 mg of **bio-MOF 11-14** samples were soaked in ~10 ml of water in a 20 ml glass vial and shaken vigorously. After 1 hour, PXRD patterns were collected for the wet samples. **Bio-MOF-14** was soaked in water for an extended period of time (7 or 30 days) and then dried under argon flow for SEM and gas adsorption studies.

Single X-ray Diffraction.

General Methods.

The crystal structures of **bio-MOF-12**, **13**, and **14** were determined by single crystal X-ray diffraction experiments. A single crystal of either **bio-MOF-12**, **13**, or **14** was loaded into a glass capillary tube (Hampton research, glass 50) with Paratone oil. X-ray diffraction data were collected on a Bruker Smart Apex CCD diffractometer with graphite-monochromated MoKα (λ = 0.71073 Å) radiation at 273 K. SMART (V 5.628) was used for data collection and SAINT was used for cell refinement and data reduction. Absorption was corrected using Bruker program SADABS built into SAINT. Structures were solved by direct methods and refined by full-matrix least-squares analysis. All the non-hydrogen atoms were found from subsequent difference Fourier syntheses and refined anisothropically (except two terminal carbon atoms on the aliphatic chain in **bio-MOF-13** and water molecules were refined isotropically) with Bruker program SHELXTL[31] (V 6.10). Ideal positions for all hydrogen atoms were calculated and refined as a rigid model (except two hydrogen atoms on the amino group in **bio-MOF-13** were generated from Fourier syntheses and refined isotropically). Detailed single crystal data tables are given in the Supporting Information.

Modeling the Disordered Aliphatic Chains.

The butyrate and valerate chains in **bio-MOF-13** and **14**, respectively, were found to be disordered. In the case of **bio-MOF-13**, the terminal ethyl group was treated with partial occupancy at two positions resulting in configuration I and configuration II with probability of 42.6 % and 57.4 %, respectively (Figure S2B). Identical thermal parameters (U_{eq}) were applied to both configurations. The terminal carbon was considered to have 20 % higher thermal parameter value than the β carbon. Except for the β, and γ carbons, the remaining non-hydrogen atoms were refined anisotropically. The aliphatic chain in **bio-MOF-14** was more severely disordered than that in **bio-MOF-13**. The disordered valerate chain was modeled as configuration I, II, and III with partial occupancies of 34.7 %, 47.6 %, and 17.7 %, respectively (Figure S3B). Soft bond restraints were applied to the valerate carbon atoms. Except for the solvent oxygen atom, the remaining non-hydrogen atoms were refined anisotropically.

Modeling Details.

Ideal adsorbed solution theory (IAST)[32] was employed to predict the adsorption isotherms of binary CO_2/N_2 mixtures with 10% CO_2, based on the pure component isotherms from experiments at 273 and 298 K. The adsorption isotherm data were fitted to a dual site Langmuir model to obtain the single component adsorption isotherms required for the IAST calculations, as described previously.[30] Plane wave periodic density functional theory (DFT) calculations were performed using the Vienna Ab initio Simulation Package (VASP).[33-36] DFT was used to compute the binding energies of CO_2 molecules in **bio-MOF-12**. The generalized gradient approximation functional of Perdew-Burke-Ernzerhof (PBE)[37] was used to describe the exchange-correlation functional; van der Waals interactions were included through use of the semi-empirical functional of Grimme (DFT-D2).[38] DFT molecular dynamics calculations at a temperature of 500 K were carried out to explore the conformational changes of the aliphatic chains in **bio-MOFs 12-14**. A cutoff energy of 400 eV and gamma point sampling of the Brillouin zone were used for all of the calculations. Classical grand canonical Monte Carlo (GCMC) simulations were carried out to model the adsorption of CO_2 in the bio-MOFs. The model of Garcia-Sanchez et al.[39] was used for CO_2-CO_2 interactions. The CO_2-framework interactions were computed using the Universal Force Field[40] parameters for the framework atoms with Lorentz-Berthelot combining rules, along with point charges for the framework atoms computed from fitting the periodic DFT electrostatic potential.[41] The potential parameters and charges used are reported in Tables S16 and S17 of the Supporting Information.

RESULTS AND DISCUSSION

Design Approach, Preparation, and Structural Characterization.

As described in a previous report[10], **bio-MOF-11**, $Co_2(ad)_2(CH_3CO_2)_2$, crystallizes in the $I4_1/a$ space group (a = b = 15.4355(18) Å, c = 22.775(5) Å; α = β = γ = 90 °). It consists of cobalt-adeninate-acetate ‘paddle-wheel’ building blocks that are periodically linked together through the N7 of the adeninate to form a 3-D structure with the augmented ***lvt*** topology.[42] This arrangement of building blocks affords channels that run parallel to the *a* and *b* crystallographic axes. These channels are densely functionalized with Lewis-basic groups: the top and bottom wall of each channel is decorated, in a zig-zag fashion, with amino groups spaced 5 Å apart as well as pyrimidal nitrogen groups spaced 4.7 Å apart. In addition, the channels are lined with methyl groups from the acetates of the building blocks.

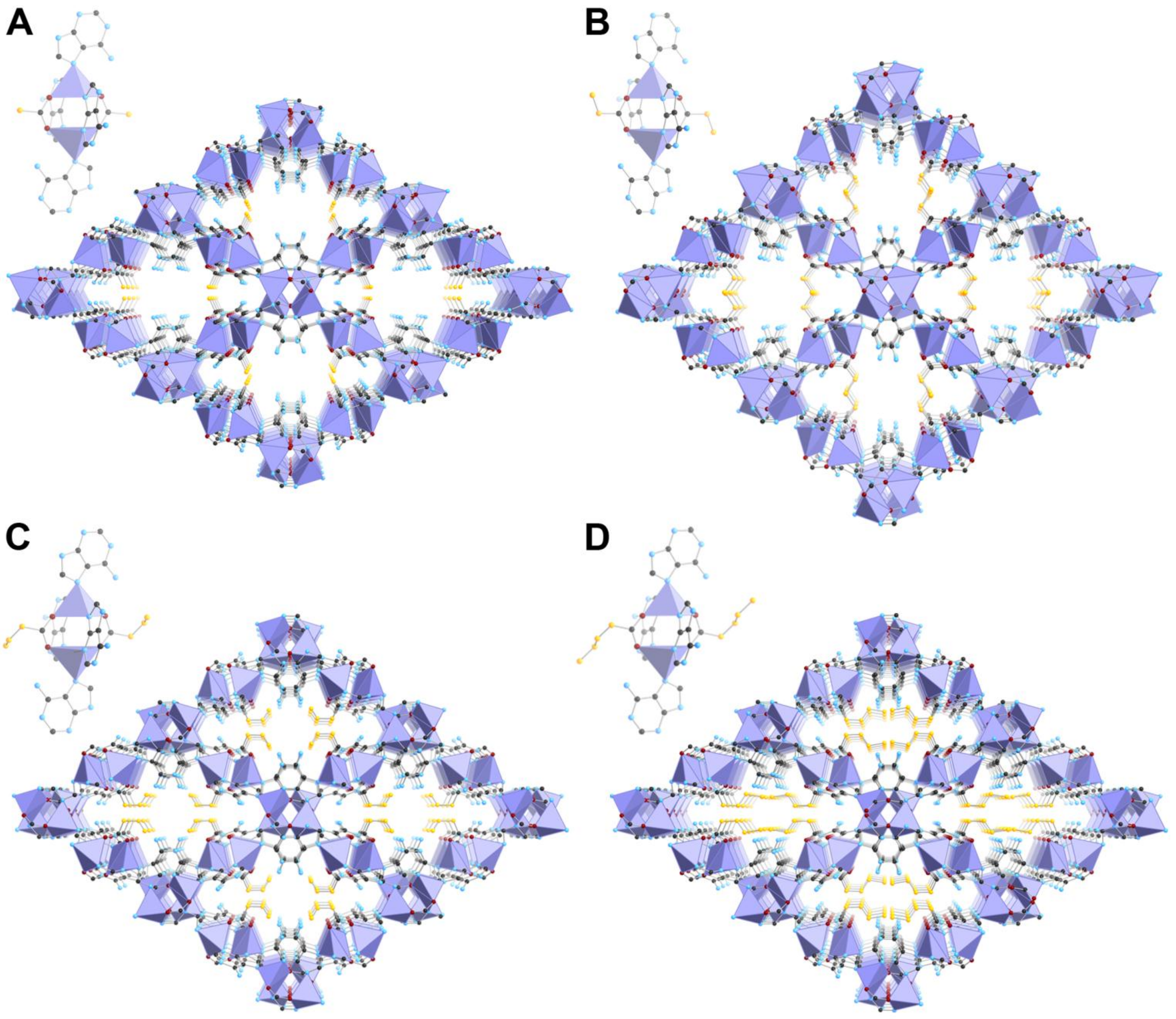

Figure 2. Secondary building units (SBUs) (upper left quadrant) and crystal structures of **bio-MOF-11**, **12**, **13**, and **14** (A, B, C, and D, respectively (Co^{2+}, light purple polyhedra; C, dark gray spheres; O, dark red spheres; N, light blue spheres. H atoms have been omitted for clarity. Aliphatic carbon atoms are represented by orange spheres).

After studying the structure of **bio-MOF-11**, we decided to fabricate an isoreticular series of MOFs by replacing the acetate groups with monocarboxylates having longer aliphatic chains, such as propionate, butyrate, and valerate. These small modifications to the **bio-MOF-11** structure would allow us to carefully modulate both the cavity size and the pore hydrophobicity. To realize this design strategy, we prepared the cobalt monocarboxylate salts (cobalt propionate, cobalt butyrate, and cobalt valerate) and then reacted these salts with adenine under solvothermal conditions. Each reaction yielded crystalline product. Collection and subsequent refinement of single crystal X-ray diffraction data for each product MOF, **bio-MOF-12** ($Co_2(ad)_2(C_2H_5CO_2)_2$), **bio-MOF-13** ($Co_2 (ad)_2(C_3H_7CO_2)_2$), and **bio-MOF-14** ($Co_2(ad)_2(C_4H_9CO_2)_2$) (Figure 2), confirmed that they were isostructural to **bio-MOF-11**.[23, 43, 44] The complete compositions of the solvated samples were determined via elemental analysis. **Bio-MOFs-12**, **13**, and **14** each crystallize in the tetragonal space group ($I4_1/a$), and the unit cells are similar to each other and to **bio-MOF-11** (Table 1). Compared to the other members of the series, the unit cell of **bio-MOF-12** is slightly elongated along *a* and *b* but compressed along *c*. These differences derive from close interactions (3.55 Å nearest neighbor distance) between the propionate methyl group and the six-member pyrimidal ring of the adeninate. The alkyl chains of

Table 1. Unit cell parameters of **bio-MOF-11** to **14**

	Unit cell parameters			
	a (Å)	b (Å)	c (Å)	$\alpha = \beta = \gamma$
Bio-MOF-11	15.44	15.44	22.78	90^o
Bio-MOF-12	17.24	17.24	20.16	90^o
Bio-MOF-13	15.79	15.79	22.33	90^o
Bio-MOF-14	15.85	15.85	22.35	90^o

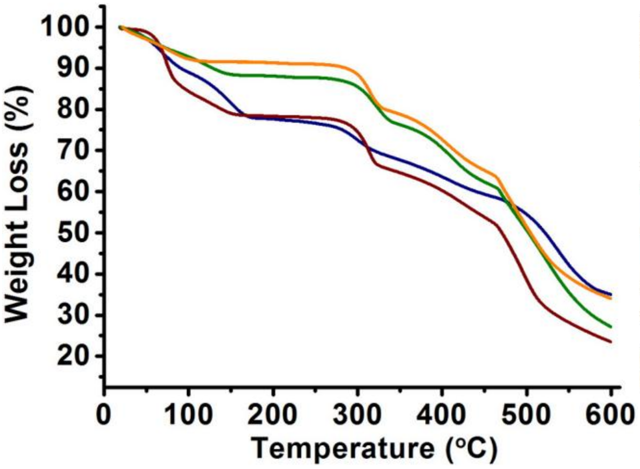

Figure 3. TGA of as-synthesized **bio-MOF-11** (navy), **bio-MOF-12** (dark red), **bio-MOF-13** (green), and **bio-MOF-14** (orange).

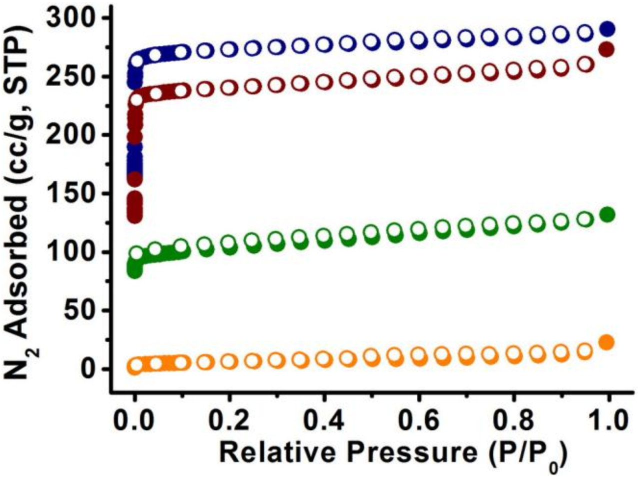

Figure 4. N_2 adsorption isotherms of **bio-MOF-11** (navy), **bio-MOF-12** (dark red), **bio-MOF-13** (green), and **bio-MOF-14** (orange) at 77 K.

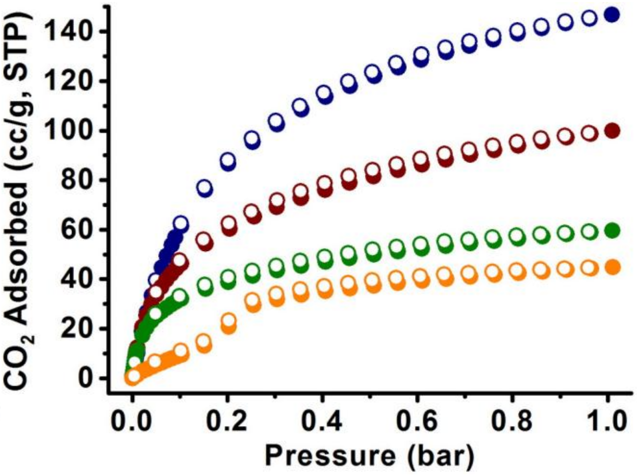

Figure 5. CO_2 adsorption isotherms of **bio-MOF-11** (navy), **bio-MOF-12** (dark red), **bio-MOF-13** (green), and **bio-MOF-14** (orange) at 273 K.

Table 2. CO_2 adsorption data and isosteric heats of adsorption at low loadings, given in parentheses.

	CO_2@273K^a	CO_2@298 K^b	Q_{st}^{c} (loading, cc/g)
Bio-MOF-11	147	105	33.1(2.18)
Bio-MOF-12	100	71	38.4(2.91)
Bio-MOF-13	60	45	40.5(3.01)
Bio-MOF-14	45	31	N/A

[a] Amount of CO_2 absorbed (cc/g) at 273 K, 1 bar. [b] Amount of CO_2 absorbed (cc/g) at 298 K, 1 bar. [c] kJ/mol.

each bio-MOF extend into the channel space with either single or multiple configurations, each of which was crystallographically resolved; these chains serve to modulate the accessible void space. Given this observation, we were keen to explore the gas adsorption properties of this series of bio-MOFs.

Porosity and N_2 Adsorption Studies.

Thermogravimetric analysis (TGA) data for as-synthesized **bio-MOFs 11-14** each exhibited a weight loss step below 200 ℃ which corresponds to the loss of DMF and water guest molecules, as determined via comparison to the elemental analysis data (Table S18). The percentage weight of included solvent decreases with the extension of the aliphatic chains: **bio-MOF-11**, 22.4 % (2.25 DMF, 0.6 H_2O); **bio-MOF-12**, 21.7 % (2.25 DMF, 0.3 H_2O); **bio-MOF-13**, 12.0 % (1.1 DMF, 0.6 H_2O); and **bio-MOF-14**, 8.7 % (0.6 DMF, 0.6 H_2O) (Figure 3, Table S18). For each material, no additional weight loss was observed until the onset of framework decomposition at approximately 280 ℃.

N_2 adsorption experiments verified the permanent porosity of **bio-MOFs 11**, **12**, and **13**. Each MOF exhibited a Type I isotherm characteristic of a microporous material (Figure 4). As expected, the surface area and pore volume decreased as the length of the aliphatic chains increases (Table S19). Surprisingly, although **bio-MOF-14** includes 8.7 wt% solvent, its N_2 uptake under the conditions studied was very low compared to the other analogues (Figure 4).

CO_2 Adsorption Studies.

We measured CO_2 isotherms for each material at multiple temperatures (Tables S20-S23). At 273 K, we found that the total CO_2 capacity at 1 bar decreased with increasing aliphatic chain length (Figure 5, Table 2). Notably, the CO_2 isotherm for **bio-MOF-14** at 273 K does not exhibit typical Langmuir behavior. Rather, it has three distinct regions: an initial gradual rise to 13 cc/g between 0 and 0.15 bar, a second steeper adsorption step to 29 cc/g between 0.15 and 0.25 bar, and a third gradual increase to 44.8 cc/g between 0.25 and 1 bar (Figure 5). Such stepwise adsorption behavior has been observed for flexible MOFs at room temperature[19, 45-51] and for rigid MOFs at low temperatures[17]. To the best of our knowledge, this behavior is unique among rigid MOFs at ambient temperature.

We collected CO_2 isotherms at higher temperatures (298, 303, 308, and 313 K) (Figures S7-S10) and used these data to calculate the isosteric heats of adsorption (Q_{st}) for **bio-MOFs 11-13**; **bio-MOF-14** Q_{st} values were not calculated because we could not fit its isotherms to the dual-site Langmuir model. **Bio-MOF-12** and **13** each have noticeably higher Q_{st} values at low loading than **bio-MOF-11** (33.1 kJ/mol for **bio-MOF-11**, 38.4 kJ/mol for **bio-MOF-12** and 40.5 kJ/mol for **bio-MOF-13**) and remain appreciably higher throughout the whole adsorption range (Figure

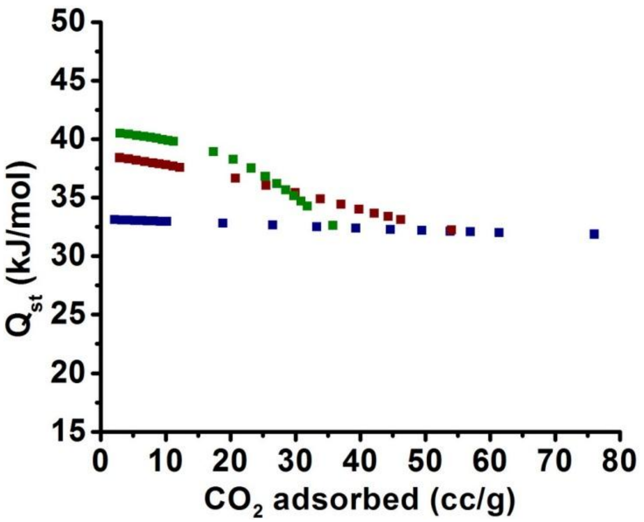

Figure 6. Isosteric heat of adsorption of **bio-MOF-11** (navy), **bio-MOF-12** (dark red), and **bio-MOF-13** (green). The absolute average errors in the Q_{st} are 0.3, 1.7, and 1.7 kJ/mol for **bio-MOF-11**, **bio-MOF-12**, and **bio-MOF-13**, respectively (details provided in the Supporting Information).

6; Table 2). The high Q_{st} values for **bio-MOF-12** and **bio-MOF-13** correlate well with the high CO_2:N_2 selectivity values computed from IAST (*vide infra*).

CO_2:N_2 Selectivity.

We first estimated the CO_2:N_2 selectivity for each bio-MOF using the single component CO_2 and N_2 isotherms. Specifically, we divided the amount of CO_2 adsorbed at 0.15 bar by the amount of N_2 adsorbed at 0.75 bar.[3] **Bio-MOF-11**, **12**, and **13** show similar selectivity ranging from 52 to 59 at 273 K and from 44 to 46 at 298 K (Figure S16). Since **bio-MOF-14** shows essentially no N_2 uptake (Figures S11 and S12), the CO_2:N_2 selectivity is predicted to be extremely high.

IAST was used to estimate the CO_2:N_2 selectivities for CO_2/N_2 gas mixtures.[32] The experimental CO_2 and N_2 isotherms collected at 273 and 298 K for **bio-MOF-11** to **13** were fitted to the dual site Langmuir model (Table S24; Figures S13-S15). We computed the IAST predicted adsorption selectivity of CO_2 over N_2 for a 10:90 CO_2/N_2 mixture (Figure 7). At 273 K, **bio-MOF-12** and **13** exhibited much higher initial CO_2:N_2 selectivity (163:1 and 290:1 respectively) than **bio-MOF-11** (102:1); they remain more selective than **bio-MOF-11** over the whole pressure range (0 - 1 bar) (Figure 7A). At 298 K, **bio-MOF-12** still exhibits an appreciably higher CO_2:N_2 selectivity (52:1) than **bio-MOF-11** (43:1) while **bio-MOF-13** exhibits a slightly lower selectivity (40:1) (Figure 7B).

It is important to understand that the inherent CO_2:N_2 selectivities for **bio-MOFs 11-13** derive principally from their Q_{st} values for CO_2 at moderate loading (*vide supra*). Indeed, the Q_{st} values (Figure 6) and the IAST selectivities (Figure 7) follow a similar trend. On the other hand, the CO_2:N_2 selectivity for **bio-MOF-14** likely derives from a molecular sieving effect (*vide infra*).

Molecular Modeling and Simulation.

To more completely understand the adsorption behavior for this series of bio-MOFs, we used Materials Studio software to generate Connolly surface diagrams for each bio-MOF. In cases where multiple aliphatic chain configurations were possible, we generated multiple diagrams. The diagrams (Figure S17-S20 and Supporting Videos 1-7) were generated using a probe radius of 1.82 Å (half the kinetic diameter of a N_2 molecule). These diagrams reveal several important pieces of information. First, they show that the cavities in **bio-MOFs 11-12** are completely interconnected and thus allow passage of N_2 molecules (Figures S17 and S18). Second, they show that when the butyrate chains in **bio-MOF-13** adopt configuration I (42.6 % occupancy), its cavities are isolated from each other; however, when they adopt configuration II (57.4 % occupancy), its cavities are interconnected (Figure S19), which leads to appreciable N_2 adsorption at 77 K (165 cc/g). Third, they show that two out of the three possible configurations of the valerate chain in **bio-MOF-14** (configuration II and III with total occupancy of 65.3 %) result in isolated cavities that would prevent passage of N_2 throughout the structure, while configuration I (34.7 %) for **bio-MOF-14** results in interconnected cavities (Figure S20). As a result, **bio-MOF-14** adsorbs a comparatively small amount of N_2 at 77 K (29 cc/g) and a negligible amount at 273 and 298 K (Figures S11 and S12). CO_2, on the other hand, has a smaller kinetic diameter (3.30 Å) than N_2 (3.64 Å)[3] and interacts more strongly with the framework. In the case of **bio-MOF-14**, a possible pressure-induced configuration change allows CO_2 to

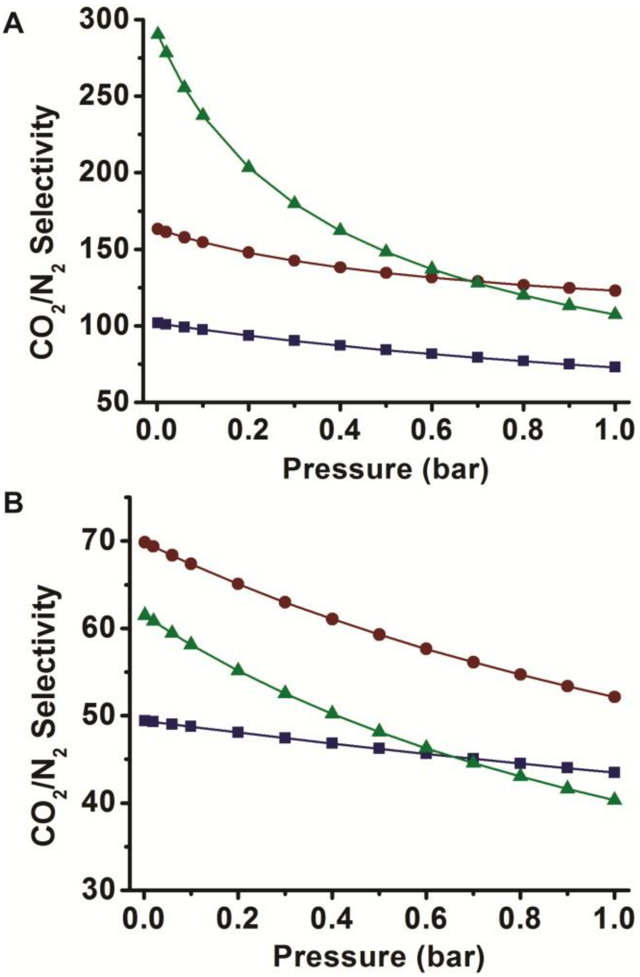

Figure 7. IAST selectivity for CO_2:N_2 (10:90 mixture) of **bio-MOF-11** (navy), **bio-MOF-12** (dark red), and **bio-MOF-13** (green) at 273 K (A) and 298 K (B).

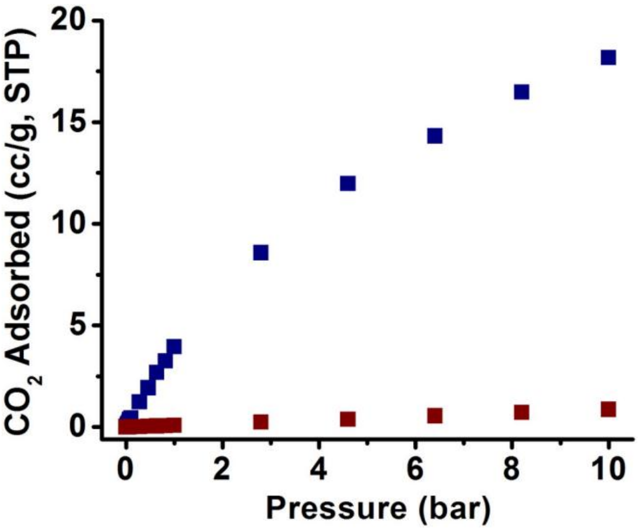

Figure 8. Adsorption isotherms at 298 K of CO$_2$ in **bio-MOF-14** from grand canonical Monte Carlo Simulations using two different configurations of the valerate chains.

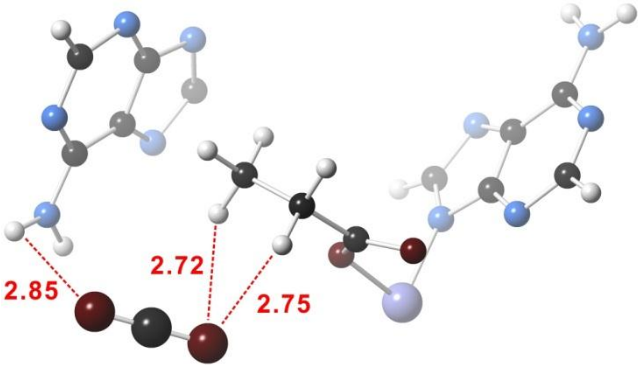

Figure 9. Ground state structure of CO$_2$ in **bio-MOF-12** as computed from DFT-D2. The dashed lines indicate Lewis acid/base interactions, with O—H bond lengths shown in angstroms (Co^{2+}, light purple spheres; C, dark gray spheres; O, dark red spheres; N, light blue spheres; H, white spheres).

access the inner cavities after the breakthrough point (Figure 5, 0.15 bar), resulting in the observed unusual CO$_2$ adsorption behavior. Our molecular modeling results support this conclusion. We have quantified the effects of configurations of the valerate chains on the adsorption isotherms by comparing adsorption isotherms computed from GCMC simulations using two different valerate configurations generated from our DFT molecular dynamics calculations that were then relaxed to their local minima. These isotherms are plotted in Figure 8. The energy difference between the two configurations is 0.065 eV per unit cell (496 atoms), with the configuration having the largest uptake having the lower energy. The configurations of the chains were held fixed in the GCMC simulations. The isotherms in Figure 8 indicate that chain configurations in **bio-MOF-14** can have a profound effect on the adsorption capacity. Moreover, the adsorption of CO$_2$ could influence the chain configuration because the energy differences between the configurations are not large. Hence, it is likely that the step in the isotherm for **bio-MOF-14** seen in Figure 5 is the result of configurational changes of the valerate chains induced by the presence of CO$_2$. In contrast, our simulations found that the configurations of the aliphatic chains in **bio-MOFs 11-13** had little effect on the computed adsorption isotherms. Note that the modelling results from the Connolly surface diagram and the GCMC simulations complement one another. The former indicates pore entrance blocking, which limits adsorption on reasonable time-scales, while the latter indicates that the chain configurations also dramatically impact equilibrium loading. To summarize, N$_2$ cannot access the pores of **bio-MOF-14** at any of the studied

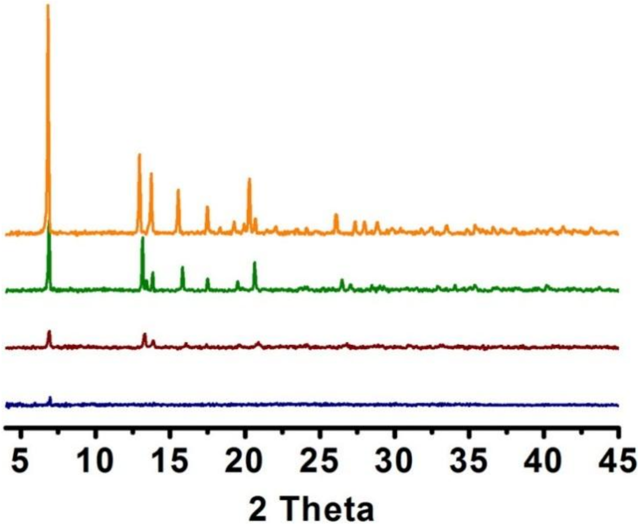

Figure 10. PXRD patterns of **bio-MOF-11** (navy), **bio-MOF-12** (dark red), **bio-MOF-13** (green), and **bio-MOF-14** (orange) after one hour soaking in water.

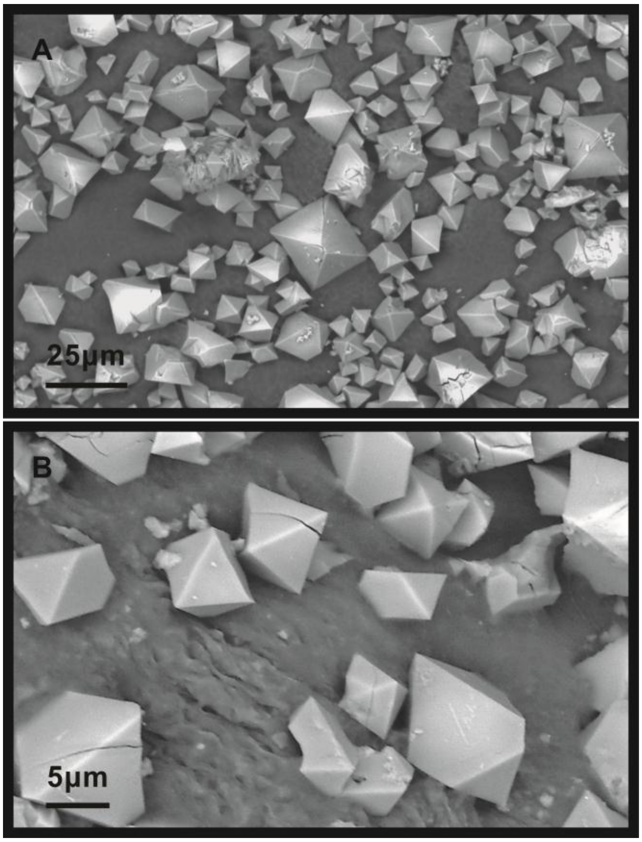

Figure 11. SEM images of **bio-MOF-14** before (A) and after (B) 1 hour soaking in water.

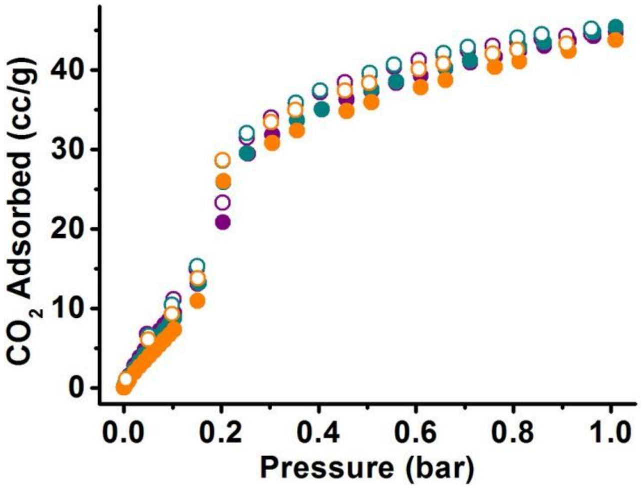

Figure 12. CO_2 isotherms of as synthesized **bio-MOF-14** (cyan), after soaking in water for 7 days (purple) and 30 days (orange).

elevated temperatures (273 and 298 K) due to a molecular sieving effect, whereas CO_2 can access the pores through a gating process.[49, 52] As a result, **bio-MOF-14** exhibits extremely high selectivity for CO_2 over N_2, as inferred from single component isotherms.

We have explored many different adsorption configurations for CO_2 within **bio-MOF-12** using the van der Waals corrected DFT-D2 approach. We did not find any indication of chemical binding or significant charge transfer complexes. The strongest interaction sites for CO_2 were not the Lewis-base sites, but the Lewis-acid sites, as seen by the computed ground state structure shown in Figure 9. Previous calculations have demonstrated how CO_2 can act as both a Lewis acid and a Lewis base when interacting with CO_2-soluble polymers,[53] so it is not surprising that similar interactions could be important in MOFs. Our calculations show that CO_2 is arranged so that it makes three Lewis-acid/Lewis-base interactions with slightly acidic protons on the framework, having O—H bond distances of 2.72, 2.75, and 2.85 Å. The binding energy of this configuration is 36 kJ/mol, which is in good agreement with the experimentally calculated isosteric heats for **bio-MOF-12**.

Water Stability Studies.

Having shown that increasing the length of the aliphatic group can positively impact CO_2:N_2 selectivity, we next explored whether the identity of the aliphatic group could impact the water stability of the respective bio-MOFs. We first soaked a sample of each bio-MOF in water for 1 hour, and then we used PXRD and SEM imaging to initially evaluate the materials' stability. **Bio-MOF-11**, as mentioned previously, dissolved rapidly in water, as evidenced by PXRD (Figure 10); SEM images could not be obtained. **Bio-MOFs 12** and **13** dissolved partially in water. The intensity of their signature diffraction lines decreased substantially (Figure 10); however, it was clear from comparing PXRD patterns that **bio-MOF-13**, with butyrate, was noticeably more stable in water than **bio-MOF-12**, with propionate (Figure 10). SEM images of the soaked samples supported this conclusion: they revealed significant crystallite fragmentation and pitting of the crystal surfaces (Figure S21), consistent with degradation, for **bio-MOF-12** samples yet only a small amount of fragmentation and pitting for **bio-MOF-13** samples (Figure S22).

Bio-MOF-14, with the valerate groups, was the most stable of the series and showed no loss of crystallinity (Figure 10) and no significant crystal degradation after soaking in water for 1 hour (Figure 11). We therefore extended the water soaking period to 7 and 30 days; the PXRD pattern shows no loss in crystallinity (Figure S24), and SEM images show only minimal pitting on the crystal surface after 7 or 30 days soaking in water (Figure S23). To further prove that the material remains intact upon extended exposure to water, we collected CO_2 isotherms at 273 K for samples of **bio-MOF-14** which were soaked in water for either 7 or 30 days (Figure 12). The isotherms are nearly identical and they closely match the isotherm of the non-water-treated sample in both shape and capacity, indicating that water does not affect the porosity of the material.

Conclusions

Herein, we have shown that small, systematic modifications of the pore space in a series of isoreticular adenine-based bio-MOFs can lead to dramatic changes in the N_2 and CO_2 adsorption properties and the water stability of the materials. Specifically, we demonstrate that the decoration of the pore environment with aliphatic chains of increasing length leads to an increase in the CO_2:N_2 selectivity and an increase in the water stability of this series of bio-MOFs. Importantly, we used this systematic approach to produce **bio-MOF-14**, which is water stable and exhibits exceptional selectivitiy for CO_2 over N_2.

Acknowledgment

As part of the National Energy Technology Laboratory's Regional University Alliance (NETL-RUA), a collaborative initiative of the NETL, this technical effort was performed under the RES contract DE-FE0004000 (NLR). This work was partially supported by the US DOE through Grant No. DE-FG02-10ER16164 (JKJ). The authors thank Dr. Steven Geib, Dr. Michael Takase and Dr. Allen Oliver for discussion on the crystal structure refinement. The authors also thank the Petersen Institute for Nanoscience and Engineering (PINSE) for access to XRPD instrumentation and the Mechanical Engineering and Materials Science (MEMS) Department for access to SEM instrumentation.

Notes and references

[a] *Department of Chemistry, University of Pittsburgh, 219 Parkman Ave, Pittsburgh, Pennsylvania 15260. E-mail: nrosi@pitt.edu*
[b] *Department of Chemical and Petroleum Engineering, University of Pittsburgh, 3700 O'Hara Street, Pittsburgh, Pennsylvania 15261*
[c] *United States Department of Energy, National Energy Technology Laboratory, 626 Cochrans Mill Road, Pittsburgh, Pennsylvania 15236*

† Electronic Supplementary Information (ESI) available: Additional isotherms, single crystal data tables, EA data, and TGA data.. See DOI: 10.1039/b000000x/

1. H. W. Pennline, D. R. Luebke, K. L. Jones, C. R. Myers, B. I. Morsi, Y. J. Heintz and J. B. Ilconich, *Fuel Process. Technol.*, 2008, **89**, 897.

2. T. C. Drage, C. E. Snape, L. A. Stevens, J. Wood, J. Wang, A. I. Cooper, R. Dawson, X. Guo, C. Satterley and R. Irons, *J. Mater. Chem.*, 2012, **22**, 2815.
3. K. Sumida, D. L. Rogow, J. A. Mason, T. M. McDonald, E. D. Bloch, Z. R. Herm, T. H. Bae and J. R. Long, *Chem. Rev.*, 2012, **112**, 724.
4. S. Keskin, T. M. van Heest and D. S. Sholl, *ChemSusChem*, 2010, **3**, 879.
5. D. Britt, H. Furukawa, B. Wang, T. G. Glover and O. M. Yaghi, *Proc. Natl. Acad. Sci. U. S. A.*, 2009, **106**, 20637.
6. R. Banerjee, H. Furukawa, D. Britt, C. Knobler, M. O'Keeffe and O. M. Yaghi, *J. Am. Chem. Soc.*, 2009, **131**, 3875.
7. T. M. McDonald, W. R. Lee, J. A. Mason, B. M. Wiers, C. S. Hong and J. R. Long, *J. Am. Chem. Soc.*, 2012, **134**, 7056.
8. A. Demessence, D. M. D'Alessandro, M. L. Foo and J. R. Long, *J. Am. Chem. Soc.*, 2009, **131**, 8784.
9. S. R. Caskey, A. G. Wong-Foy and A. J. Matzger, *J. Am. Chem. Soc.*, 2008, **130**, 10870.
10. J. An, S. J. Geib and N. L. Rosi, *J. Am. Chem. Soc.*, 2010, **132**, 38-39.
11. R. Vaidhyanathan, S. S. Iremonger, K. W. Dawson and G. K. Shimizu, *Chem. Commun*, 2009, 5230.
12. S. S. Iremonger, J. Liang, R. Vaidhyanathan, I. Martens, G. K. H. Shimizu, T. D. Daff, M. Z. Aghaji, S. Yeganegi and T. K. Woo, *J. Am. Chem. Soc.*, 2011, **133**, 20048.
13. S. Xiang, Y. He, Z. Zhang, H. Wu, W. Zhou, R. Krishna and B. Chen, *Nat. Commun.*, 2012, **3**, 954.
14. S. D. Burd, S. Ma, J. A. Perman, B. J. Sikora, R. Q. Snurr, P. K. Thallapally, J. Tian, L. Wojtas and M. J. Zaworotko, *J. Am. Chem. Soc.*, 2012, **134**, 3663.
15. J. J. Gassensmith, H. Furukawa, R. A. Smaldone, R. S. Forgan, Y. Y. Botros, O. M. Yaghi and J. F. Stoddart, *J. Am. Chem. Soc.*, 2011, **133**, 15312.
16. Y.-S. Bae, O. K. Farha, J. T. Hupp and R. Q. Snurr, *J. Mater. Chem.*, 2009, **19**, 2131.
17. S. Yang, X. Lin, W. Lewis, M. Suyetin, E. Bichoutskaia, J. E. Parker, C. C. Tang, D. R. Allan, P. J. Rizkallah, P. Hubberstey, N. R. Champness, K. Mark Thomas, A. J. Blake and M. Schröder, *Nat. Mater.*, 2012, **11**, 710.
18. B. Li, Z. Zhang, Y. Li, K. Yao, Y. Zhu, Z. Deng, F. Yang, X. Zhou, G. Li, H. Wu, N. Nijem, Y. J. Chabal, Z. Lai, Y. Han, Z. Shi, S. Feng and J. Li, *Angew. Chem., Int. Ed.*, 2012, **51**, 1412.
19. P. K. Thallapally, J. Tian, M. Radha Kishan, C. A. Fernandez, S. J. Dalgarno, P. B. McGrail, J. E. Warren and J. L. Atwood, *J. Am. Chem. Soc.*, 2008, **130**, 16842.
20. Q. Lin, T. Wu, S.-T. Zheng, X. Bu and P. Feng, *J. Am. Chem. Soc.*, 2011, **134**, 784.
21. K. L. Kauffman, J. T. Culp, A. J. Allen, L. Espinal, W. Wong-Ng, T. D. Brown, A. Goodman, M. P. Bernardo, R. J. Pancoast, D. Chirdon and C. Matranga, *Angew. Chem., Int. Ed.*, 2011, **50**, 10888.
22. R. Luebke, J. F. Eubank, A. J. Cairns, Y. Belmabkhout, L. Wojtas and M. Eddaoudi, *Chem. Commun*, 2012, **48**, 1455.
23. J.-R. Li, Y. Ma, M. C. McCarthy, J. Sculley, J. Yu, H.-K. Jeong, P. B. Balbuena and H.-C. Zhou, *Coord. Chem. Rev.*, 2011, **255**, 1791.
24. J. R. Li, J. Sculley and H. C. Zhou, *Chem. Rev.*, 2012, **112**, 869.
25. J. An, O. K. Farha, J. T. Hupp, E. Pohl, J. I. Yeh and N. L. Rosi, *Nat. Commun.*, 2012, **3**, 604.
26. J. An, R. P. Fiorella, S. J. Geib and N. L. Rosi, *J. Am. Chem. Soc.*, 2009, **131**, 8401.
27. J. An, S. J. Geib and N. L. Rosi, *J. Am. Chem. Soc.*, 2009, **131**, 8376.
28. J. An and N. L. Rosi, *J. Am. Chem. Soc.*, 2010, **132**, 5578.
29. J. An, C. M. Shade, D. A. Chengelis-Czegan, S. p. Petoud and N. L. Rosi, *J. Am. Chem. Soc.*, 2011, **133**, 1220.
30. S. Keskin, J. Liu, J. K. Johnson and D. S. Sholl, *Langmuir*, 2008, **24**, 8254.
31. G. Sheldrick, *Acta Crystallogr., Sect. A*, 2008, **64**, 112.
32. A. L. Myers and J. M. Prausnitz, *AIChE J.*, 1965, **11**, 121.
33. G. Kresse and J. Hafner, *Phys. Rev. B*, 1993, **47**, 558.
34. G. Kresse and J. Hafner, *Phys. Rev. B*, 1994, **49**, 14251.
35. G. Kresse and J. Furthmüller, *Comput. Mater. Sci.*, 1996, **6**, 15.
36. G. Kresse and J. Furthmüller, *Phys. Rev. B*, 1996, **54**, 11169.
37. J. P. Perdew, K. Burke and M. Ernzerhof, *Phys. Rev. Lett.*, 1996, **77**, 3865.
38. S. Grimme, *J. Comput. Chem.*, 2006, **27**, 1787.
39. A. García-Sánchez, C. O. Ania, J. B. Parra, D. Dubbeldam, T. J. H. Vlugt, R. Krishna and S. a. Calero, *J. Phys. Chem. C*, 2009, **113**, 8814.
40. A. K. Rappe, C. J. Casewit, K. S. Colwell, W. A. Goddard and W. M. Skiff, *J. Am. Chem. Soc.*, 1992, **114**, 10024.
41. D.-L. Chen, A. C. Stern, B. Space and J. K. Johnson, *J. Phys. Chem. A*, 2010, **114**, 10225.
42. O. Delgado Friedrichs, M. O'Keeffe and O. M. Yaghi, *Acta Crystallogr., Sect. A*, 2003, **59**, 515.
43. After we completed the comprehensive studies reported herein, a series of isostructural Cu-adeninate frameworks were reported. S. Pérez-Yáñez, G. Beobide, O. Castillo, J. Cepeda, A. Luque, A. s. T. Aguayo and P. Román, *Inorg. Chem.*, 2011, **50**, 5330.
44. S. Pérez-Yáñez, G. Beobide, O. Castillo, J. Cepeda, A. Luque and P. Román, *Cryst. Growth & Des.*, 2012, **12**, 3324.
45. H. Wu, R. S. Reali, D. A. Smith, M. C. Trachtenberg and J. Li, *Chem.--Eur. J.*, 2010, **16**, 13951.
46. A. Ghoufi, A. Subercaze, Q. Ma, P. G. Yot, Y. Ke, I. Puente-Orench, T. Devic, V. Guillerm, C. Zhong, C. Serre, G. Férey and G. Maurin, *J. Phys. Chem. C*, 2012, **116**, 13289.
47. D. Li and K. Kaneko, *Chem. Phys. Lett.*, 2001, **335**, 50.
48. A. R. Millward and O. M. Yaghi, *J. Am. Chem. Soc.*, 2005, **127**, 17998.
49. S. Henke and R. A. Fischer, *J. Am. Chem. Soc.*, 2011, **133**, 2064.
50. H. J. Park and M. P. Suh, *Chem. Commun*, 2010, **46**, 610.
51. H.-S. Choi and M. P. Suh, *Angew. Chem., Int. Ed.*, 2009, **48**, 6865.
52. J. Seo, R. Matsuda, H. Sakamoto, C. Bonneau and S. Kitagawa, *J. Am. Chem. Soc.*, 2009, **131**, 12792.
53. Y. Wang, L. Hong, D. Tapriyal, I. C. Kim, I.-H. Paik, J. M. Crosthwaite, A. D. Hamilton, M. C. Thies, E. J. Beckman, R. M. Enick and J. K. Johnson, *J. Phys. Chem. B*, 2009, **113**, 14971.